

The Momentum Distribution of Liquid ^4He

T. R. Prisk¹  · M. S. Bryan² · P. E. Sokol² ·
G. E. Granroth³ · S. Moroni⁴ · M. Boninsegni⁵

Received: 26 May 2017 / Accepted: 10 July 2017 / Published online: 24 July 2017
© Springer Science+Business Media, LLC (outside the USA) 2017

Abstract In this paper, we report a high-resolution neutron Compton scattering study of liquid ^4He under milli-Kelvin temperature control. To interpret the scattering data, we performed Quantum Monte Carlo calculations of the atomic momentum distribution and final state effects for the conditions of temperature and density considered in the experiment. There is excellent agreement between the observed scattering and ab initio calculations of its lineshape at all temperatures. We also used model fit functions to obtain from the scattering data empirical estimates of the average atomic kinetic energy and Bose condensate fraction. These quantities are also in excellent agreement with ab initio calculations. We conclude that contemporary Quantum Monte Carlo methods can furnish accurate predictions for the properties of Bose liquids, including the condensate fraction, close to the superfluid transition temperature.

Keywords Bose–Einstein condensation · Momentum distributions · Inelastic neutron scattering · Quantum Monte Carlo

✉ T. R. Prisk
timothy.prisk@nist.gov

¹ Center for Neutron Research, National Institute of Standards and Technology, Gaithersburg, MD 20899-6100, USA

² Department of Physics, Indiana University, Bloomington, IN 47408, USA

³ Neutron Data Analysis and Visualization Division, Oak Ridge National Laboratory, Oak Ridge, TN 37831, USA

⁴ CNR-IOM DEMOCRITOS, Istituto Officina dei Materiali, and SISSA Scuola Internazionale Superiore di Studi Avanzati, Via Bonomea 265, 34136 Trieste, Italy

⁵ Department of Physics, University of Alberta, Edmonton, AB T6G 2E1, Canada

1 Introduction

Bose condensation plays an important role in contemporary quantum many-body physics. It is generally believed to provide the microscopic basis for superfluidity in bulk liquid ^4He [1–3]. On this view, the local order parameter of the normal-to-superfluid phase transition is a macroscopic wavefunction describing the motion of the condensate. The spontaneously broken gauge symmetry produces many fundamental properties of superfluid ^4He , such as its two-fluid hydrodynamics, critical exponents, and quantization of circulation. Recent interest in Bose condensation encompasses a broad range of topics [4], including dilute atomic gases [5], solid state excitations [6–11], nonlinear optical systems [12, 13], neutron stars [14], and gravitation [15–17]. Among these Bose-condensed systems, bulk superfluid ^4He represents the strongly interacting limit due to the steeply repulsive core of its interatomic potential.

The study of Bose broken symmetry in superfluid ^4He is therefore a subject of fundamental interest in quantum many-body physics. The only known physical property of liquid ^4He that can provide direct information about the existence and magnitude of its Bose condensate is the atomic momentum distribution $n(k)$. Hohenberg and Platzman originally proposed that neutron Compton scattering be used to measure the momentum distribution $n(k)$ of liquid ^4He [18]. Their proposal stimulated many experimental efforts to determine the Bose condensate fraction n_0 and average atomic kinetic energy $\langle E_K \rangle$ throughout the phase diagram of ^4He [19–23]. Several groups have performed measurements of $n(k)$ using the high fluxes of epithermal neutrons available at modern spallation sources. This includes the MARI [24–29], PHOENIX [30–34], and eVS [35] spectrometers.

The first ab initio calculations of $n(k)$ at finite temperatures were carried out using the Path Integral Monte Carlo method [36–38]. However, this pioneering study was limited by the small system size, resulting in significant finite-size rounding of the superfluid phase transition. Improvements in Quantum Monte Carlo methods, based upon the continuous space worm algorithm [39, 40], now permit much larger system sizes to be studied. This makes available a more detailed theoretical picture, particularly for temperatures close to T_λ , than was possible previously. However, the new theoretical predictions for the temperature dependence of the Bose condensate fraction n_0 have yet to face a strenuous test.

In this paper, we present a comprehensive theoretical and experimental study of the momentum distribution $n(k)$ of bulk liquid ^4He under saturated vapor pressure. We performed high-resolution neutron Compton scattering measurements of liquid ^4He under fine temperature control using the Wide Angular Range Chopper Spectrometer (ARCS) at the Spallation Neutron Source [41]. To interpret the scattering data, we performed Quantum Monte Carlo (QMC) calculations of the atomic momentum distribution $n(k)$ by means of the continuous space worm algorithm. We accounted for corrections to the Impulse Approximation (IA) by using the theories of Silver [42, 43] and Carraro–Koonin [44, 45]. These calculations were performed for the exact same conditions of temperature and density as the experimental ones. We find that there is excellent agreement between the ARCS data set and ab initio predictions of the scattering.

The paper is organized as follows. In Sect. 2, we review the conceptual framework of neutron Compton scattering and describe the theoretically expected scattering. Section 3 provides the details of the experimental setup, instrument characterization, and data treatment. Section 4 presents the experimental data without any reference to theoretical models. In Sect. 5, we compare our experimental data to theoretical predictions. We also use model fit functions to obtain empirical estimates of the average atomic kinetic energy $\langle E_K \rangle$ and condensate fraction n_0 as a function of temperature. The scattering data collected by the PHOENIX group is re-analyzed using the present models. Lastly, we state our main findings in the Conclusion.

2 Theoretical Background

2.1 One-Body Density Matrix

The formal definition of Bose condensation in a strongly interacting system is given in terms of the one-body density matrix $\tilde{n}(s)$ [1, 3]. This quantity is the expectation value of the product of a particle creation operator at \mathbf{s} and a particle annihilation operator at the origin: $\tilde{n}(s) = \langle \Psi^\dagger(\mathbf{s})\Psi(0) \rangle$. At zero temperature, $\tilde{n}(s)$ measures the overlap in the many-body wavefunction of the system when a particle is removed from the origin and then placed some distance s away. A system is Bose-condensed if and only if $\tilde{n}(s)$ approaches a constant value, n_0 , as $s \rightarrow \infty$. The atomic momentum distribution $n(k)$ is the Fourier transform of the one-body density matrix $\tilde{n}(s)$. Accordingly, the Bose condensate appears in $n(k)$ as a δ -function located at $k = 0$ with an integrated intensity of n_0 .

The one-body density matrix $\tilde{n}(s)$ of an interacting Bose system as a function of temperature can be computed from first principles, i.e., directly from a microscopic Hamiltonian making use of a realistic potential to describe the interaction among atoms, by means of Quantum Monte Carlo simulations. In particular, the worm algorithm (WA) in continuous space [39, 40], based on Feynman's space-time formulation of quantum statistical mechanics [46], has emerged over the past decade as a powerful methodology, allowing one to calculate accurate equilibrium thermodynamics of Bose systems. The values of the physical estimates can be regarded as *exact*, at least for practical purposes, as the statistical and systematic uncertainties (the latter arising from the finite size of the simulated system) affecting them can be rendered in practice negligibly small with the typical computing resources available nowadays.

Because this numerical technique, which is by now fairly well established, is extensively described elsewhere [39, 40], we do not review it here. Rather, we merely furnish the relevant technical details. The results presented here were obtained by simulating an ensemble of $N = 256$ ^4He atoms enclosed in a cubic vessel, with periodic boundary conditions. We used the standard microscopic model of ^4He , based on the Aziz pair potential [47, 48]. In principle, a more complete microscopic description of the system should include contributions to the potential energy associated not just with pairs, but also with, e.g., triplets of atoms. Indeed, such contributions are known to play an important role when it comes to reproducing theoretically the experimental equation of state of liquid ^4He , but their effect of the single-particle dynamics (e.g., the kinetic

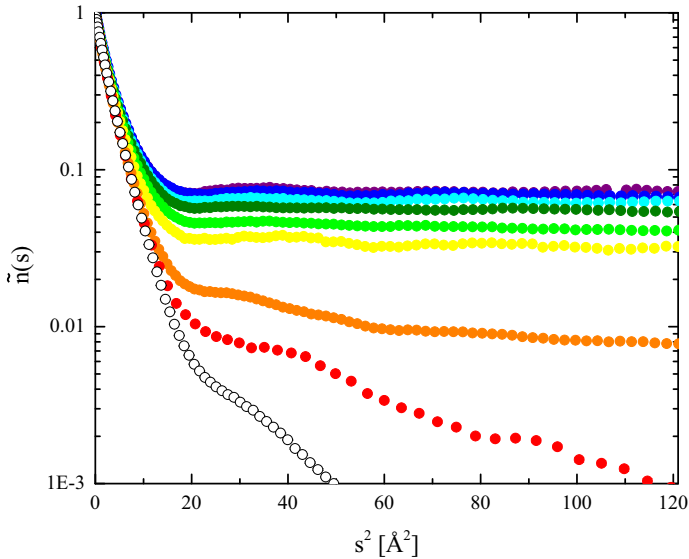


Fig. 1 QMC calculations of the one-body density matrix $\tilde{n}(s)$ of liquid ^4He under saturated vapor pressure: 1.09 K (purple), 1.40 K (blue), 1.65 K (cyan); 1.80 K (dark green), 2.00 K (light green), 2.10 K (yellow), 2.35 K (orange), 2.65 K (red), 4.2 K (open circles). Errors are smaller than symbol size (Color figure online)

energy) has been shown to be relatively small [49, 50]. Thus, the neglect of three (and higher) body terms in the Hamiltonian, in a theoretical calculation aiming mainly at reproducing the value of the condensate fraction, is widely regarded as justified.

Our simulations are carried out at fixed density, using a canonical variant of the WA [51, 52]; the values of the density corresponding to the various temperatures (in the range $0.5 \leq T \leq 2.65$ K) are taken from Ref. [53]. We report results extrapolated to the limit of vanishing imaginary time step τ (see Ref. [40] for details). In general, results obtained with $\tau = 1/640 \text{ K}^{-1}$ are indistinguishable from the extrapolated ones, within the statistical uncertainty of the calculation. We estimate the potential energy contribution arising from particles outside the main simulation cell by setting the pair correlation function $g(r)$ to unity outside the cell; which is an excellent approximation for the system size utilized in this work. The value of the ground state energy extrapolated to temperature $T = 0$ is $-7.182 \pm 0.013 \text{ K}$ per ^4He atom, indistinguishable from the estimate at the lowest temperature considered here ($T = 0.5 \text{ K}$), within statistical uncertainties.

Figure 1 plots the calculated one-body density matrix $\tilde{n}(s)$ for the conditions of our experiment. Differences between the normal and superfluid phases are evident. In the normal fluid, $\tilde{n}(s)$ decays toward zero at large s ; in the superfluid, $\tilde{n}(s)$ reaches a constant value n_0 at large s . The condensate fraction n_0 varies rapidly just below T_λ and approaches a constant value around 1 K. The estimate at $T = 1.09 \text{ K}$ is 0.075(2), which is consistent with that of Ref. [40]. The extrapolated $T = 0$ value is 0.076(2), also consistent, within the quoted statistical uncertainties, with the estimate provided in Ref. [49]. In general, the estimates furnished here are consistent with those of

Ref. [40], but the ones offered here were obtained for the values of the density and temperatures of the present experiment.

The average atomic kinetic energy $\langle E_K \rangle$ is given by the curvature of $\tilde{n}(s)$ at $s = 0$. Specifically, $\langle E_K \rangle = -(\hbar^2/2m)\nabla^2\tilde{n}(s)$, the Laplacian being evaluated at $s = 0$. Theoretical predictions for the average kinetic energy $\langle E_K \rangle$ and condensate fraction n_0 are given in Tables 1 and 2, respectively.

2.2 Neutron scattering and the Incoherent Approximation

Here we review the theoretical basis for neutron Compton scattering studies of liquid ^4He [18, 21, 22]. One measures the double-differential scattering cross section in an inelastic neutron scattering experiment:

$$\frac{d^2\sigma}{d\Omega dE} = b_{\text{coh}}^2 \frac{k_f}{k_i} S(Q, E). \quad (1)$$

Here b_{coh} is the coherent scattering length of ^4He and k_i (k_f) is the incident (final) neutron wavevector. There is no incoherent contribution to the scattering from changes in the spin state of the ^4He nucleus ($b_{\text{inc}} = 0$). The dynamic structure factor $S(Q, E)$

Table 1 Values of the average atomic kinetic energy $\langle E_K \rangle$ estimated from the ARCS data set

T (K)	$\langle E_K \rangle$ (K)	QMC (K)
1.090(10)	14.3(3)	14.17(2)
1.400(10)	14.4(5)	14.32(2)
1.650(4)	14.6(6)	14.46(2)
1.800(4)	14.6(4)	14.66(2)
2.000(4)	14.9(6)	15.08(3)
2.100(4)	15.2(3)	15.39(5)
2.35(3)	16.6(1.3)	16.09(2)
2.650(15)	16.4(5)	16.22(1)

Table 2 Values of the condensate fraction n_0 estimated from the ARCS data set

T (K)	Model A	Model B	QMC
1.090(10)	0.073(2)	0.070(4)	0.075(2)
1.400(10)	0.071(6)	0.073(6)	0.069(2)
1.650(4)	0.051(13)	0.05(2)	0.063(2)
1.800(4)	0.061(3)	0.056(3)	0.056(2)
2.000(4)	0.039(6)	0.043(10)	0.041(2)
2.100(4)	0.034(3)	0.032(4)	0.034(2)
2.35(3)	–	–	0
2.650(15)	0.000(1)	0.002(3)	0
4.20	–	–	0

of a quantum liquid is the Fourier transform of its time-dependent density–density correlation function.

$$S(\mathbf{Q}, E) = \frac{1}{2\pi N} \int_{-\infty}^{+\infty} e^{iEt/\hbar} \langle \rho(\mathbf{Q}, t) \rho^\dagger(\mathbf{Q}, 0) \rangle dt. \tag{2}$$

We may distinguish between two different regimes of Q and E transfer. At low $Q (< 4 \text{ \AA}^{-1})$, the measured scattering is dominated by coherent interference between particles and hence the collective excitations (the phonon-roton modes) of the liquid are observed [54, 55]. At high $Q (> 10 \text{ \AA}^{-1})$ the coherent interference between different particles is canceled by rapid phase variations. The scattering is now dominated by single-particle excitations. Therefore, the incoherent approximation is used to reduce the dynamic structure factor to

$$S^{(i)}(Q, E) = \frac{1}{2\pi} \int_{-\infty}^{+\infty} e^{iEt/\hbar} \langle e^{-\mathbf{Q}\cdot\mathbf{r}(t)} e^{i\mathbf{Q}\cdot\mathbf{r}(0)} \rangle dt. \tag{3}$$

At high Q , the central moments of the scattering obey the following sum rules [56]:

$$\text{Normalization: } \int_{-\infty}^{+\infty} S(Q, E) dE = 1. \tag{4}$$

$$f\text{-sum rule: } \int_{-\infty}^{+\infty} (E - E_R) S(Q, E) dE = 0. \tag{5}$$

$$\omega^2\text{-sum rule: } \int_{-\infty}^{+\infty} (E - E_R)^2 S(Q, E) dE = \frac{4}{3} E_R \langle E_K \rangle. \tag{6}$$

Here $E_R = \hbar^2 Q^2 / 2m$ is the recoil energy of a helium atom.

2.3 Impulse Approximation

The Impulse Approximation (IA) assumes that the kinetic energy transferred by an incident neutron to an individual helium atom during a scattering event is so large that the potential energy of the atom in both its initial and final states may be neglected. The IA is valid at infinite Q so long as the interatomic potential does not contain a hard core. Within the IA, $S^{(i)}(Q, E)$ reduces to an integral transform of the momentum distribution $n(k)$:

$$S_{IA}(Q, E) = \int n(\mathbf{k}) \delta \left(E - \frac{\hbar^2 Q^2}{2m} - \frac{\mathbf{k} \cdot \mathbf{Q}}{m} \right) d\mathbf{k}. \tag{7}$$

Here $n(\mathbf{k})$ is the atomic momentum distribution. When the IA is satisfied, a constant Q cut of the dynamic structure factor $S_{IA}(Q, E)$ consists of a single peak symmetric about the recoil energy $E_R = \hbar^2 Q^2 / 2m$. The width of the peak is proportional to the product of Q and the width of $n(k)$. The sum rules of incoherent scattering also apply at infinite Q , as the IA is a special case of the incoherent approximation.

Typically, the scattering data is presented and analyzed in terms of the West scaling variable Y and the neutron Compton profile $J(Y, Q)$ [57]. These quantities are defined as follows:

$$Y = \frac{m}{\hbar^2 Q} \left(E - \frac{\hbar^2 Q^2}{2m} \right). \quad (8a)$$

$$J(Y, Q) = \frac{\hbar^2 Q}{m} S(Q, E). \quad (8b)$$

If the IA is valid, then the neutron Compton profile $J_{IA}(Y)$ is related to the atomic momentum distribution $n(\mathbf{k})$ by a Radon transform [23]. The atomic momentum distribution of a Bose-condensed fluid may be expressed as a sum: $n(\mathbf{k}) = n_0\delta(\mathbf{k}) + n^*(\mathbf{k})$, where the δ -function singularity is due to the condensate. Expressing 7 in terms of the scaling variable Y yields:

$$J_{IA}(Y) = n_0\delta(Y) + 2\pi \int_{|Y|}^{\infty} kn^*(k)dk. \quad (9)$$

There are several advantages to analyzing the scattering data in terms of the scaling variable Y . First, the neutron Compton profile $J(Y, Q)$ is a one-dimensional projection of the momentum distribution $n(\mathbf{k})$. In the IA, the Y -scaling variable has the physical interpretation of being the component k_{\parallel} of the atomic momentum that is parallel to the momentum transfer \mathbf{Q} from the incident neutron $k_{\parallel} = \mathbf{k} \cdot \hat{\mathbf{Q}}$. The West scaling variable Y is also the Fourier conjugate of the distance s traveled by a recoiling helium atom. Second, if $J(Y, Q)$ is overplotted for multiple values of Q , then the points will collapse on to a single curve. Such behavior is necessary, but not sufficient, to demonstrate the applicability of the IA.

The scattering in the IA-limit is obtained from the one-body density matrix $\tilde{n}(s)$ by a Fourier cosine transform. Figure 2 compares $J_{IA}(Y)$ at 1.09 K and 2.65 K. The most striking feature of $J_{IA}(Y)$ in the superfluid phase is the δ -function singularity at $Y = 0$.

2.4 Final State Effects

The straightforward predictions of the IA turn on the assumption that a target helium atom recoils freely from the impact of a high energy neutron. However, the interatomic potential has a steeply repulsive core at short distances, making interactions of the recoiling atom with its neighbors important even at high Q . The resulting deviations from the IA are known as Final State Effects (FSE). Hohenberg and Platzman argued that the FSE broadening is governed by the ${}^4\text{He}$ - ${}^4\text{He}$ scattering cross section $\sigma(Q)$ [18,58]. They estimated that the condensate peak would be broadened by an amount roughly equal to $\rho\sigma(Q)$, where ρ is the number density of the liquid. For $Q = 30 \text{ \AA}^{-1}$, the broadening is on the order of 0.7 \AA^{-1} , which is not small compared to the expected width of $J_{IA}(Y)$, namely $\approx 2 \text{ \AA}^{-1}$. At intermediate Q , one observes oscillations in the recoil peak position and width that track the glory oscillations of $\sigma(Q)$. These Compton defects have been interpreted as evidence that FSE are in fact governed by $\sigma(Q)$ [19,59].

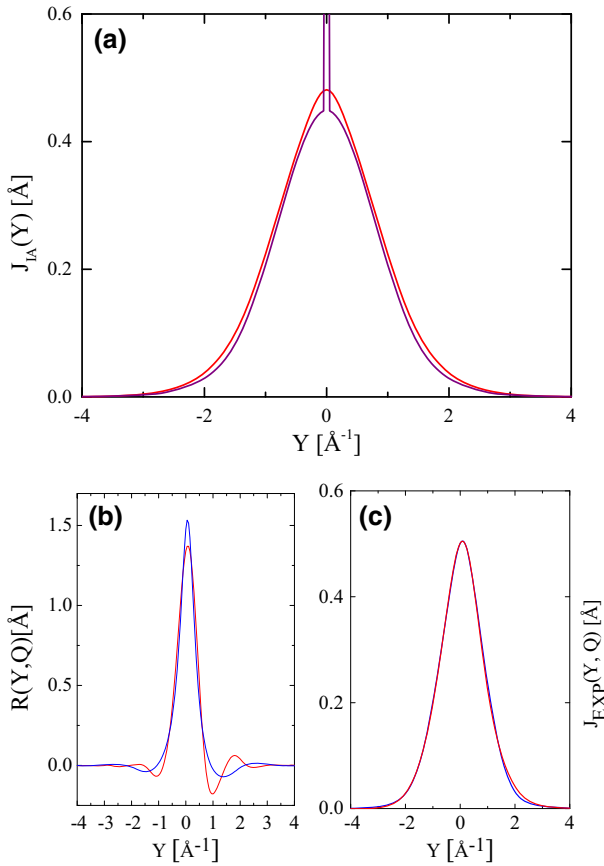


Fig. 2 **a** Expected IA-scattering $J_{IA}(Y)$ at temperatures of 2.65 and 1.09 K. **b** Comparison of final state effect functions $R(Y, Q)$ at $Q = 27.0 \text{\AA}^{-1}$ and a liquid number density $\rho = 0.02187 \text{\AA}^{-3}$. Curves Hard Core Perturbation Theory (blue); Carraro–Koonin theory (red). **c** The expected scattering $J_{EXP}(Y, Q)$ at $T = 1.09$ K when the IA is broadened by final state effects and instrumental resolution (Color figure online)

Several theoretical approaches to understanding final state effects have been proposed. In general, these approaches fall into one of three categories. The first treat final state effects as a convolution with the IA-scattering. This approach has been followed by Gersch and Rodriguez [60–63], Silver [42, 43, 64], Carraro and Koonin [44, 45] and Glyde [22]. A second approach, which has been used by Sears [57], treats final state effects as an additive correction to the IA-scattering. Finally, there are theories that treat final state effects by other methods such as alternate scaling variables [65]. A detailed comparison of these theories is beyond the scope of this work, but further discussion may be found elsewhere [22, 66–68].

We will focus on the theories that treat final state effects in terms of a broadening function:

$$J_{FS}(Y, Q) = \int_{-\infty}^{+\infty} J_{IA}(Y')R(Y - Y', Q)dY'. \tag{10}$$

where $R(Y, Q)$ is the final state broadening function. Such theories can be separated into two classes: those that calculate $R(Y, Q)$ a priori from known quantities, such as the interatomic potential and pair-distribution function, and those where the parameters of $R(Y, Q)$ must be obtained from the scattering. We examine the theories of Silver and Carraro and Koonin since they provide concrete, testable predictions for the form of $R(Y, Q)$.

The sum rules for incoherent scattering place constraints on the neutron Compton profile $J(Y, Q)$ and the FSE function $R(Y, Q)$. These rules require that $J(Y, Q)$ and $R(Y, Q)$ both be normalized to unity and have a zero first moment. The second moment of these functions must satisfy:

$$\int_{-\infty}^{+\infty} Y^2 J(Y, Q) dY = \frac{2m}{3\hbar^2} \langle E_K \rangle. \quad (11a)$$

$$\int_{-\infty}^{+\infty} Y^2 R(Y, Q) dY = 0. \quad (11b)$$

The ω^2 -sum rule implies that the second moment of $R(Y, Q)$ is identically zero. This means that $R(Y, Q)$ cannot be represented by a simple, positive-definite function, such as a Gaussian or a Lorentzian. Instead, $R(Y, Q)$ must assume both positive and negative values. The effect of convoluting $J_{IA}(Y)$ with $R(Y, Q)$ is not only to broaden the condensate peak, but also to redistribute intensity around the spectrum so that the second moment of the scattering is unaffected.

Silver developed a model lineshape $R_S(Y, Q)$ for the FSE corrections in liquid ^4He using Hard Core Perturbation Theory [21, 42, 43]. The theory takes the interatomic potential and pair-distribution function as inputs. An intuitive picture underlies Silver's theory. Before the scattering event, each helium atom is located near the minimum of the potential well generated by its nearest neighbors and far from the repulsive cores responsible for final state effects. During the impact of a high energy incident neutron, the recoiling helium atom travels a distance s , over which it may encounter the steeply repulsive cores of its neighbors. On this theory, the scaling variable Y is conjugate to the recoil distance s , although Y is no longer identical to k_{\parallel} . The FSE broadening function $R_S(Y, Q)$ is related to the Fourier transform of the classical scattering probability of suffering no collisions as a function of the travel distance s .

Carraro and Koonin developed an alternative theory $R_{CK}(Y, Q)$ for FSE corrections [44]. The starting point of their calculation is a Jastrow approximation to the many-body wavefunction of liquid ^4He . They calculate the propagator for a single atom moving at a high Q within the static potential generated by the instantaneous configuration of background atoms, and the result is averaged over many configurations distributed according to the variational wavefunction. As in Silver's model, the scaling variable Y has the physical interpretation of being the Fourier conjugate variable to the travel distance s . Here, we use an improved scheme whereby the background atoms are distributed according to a better approximation to the exact ground state than afforded by a Jastrow wavefunction. Details are given in Ref. [45]. We have calculated $R_S(Y, Q)$ and $R_{CK}(Y, Q)$ using the Aziz potential [47].

These final state effect theories are designed for the ground state. We assume that the temperature dependence of the Compton profile $J_{\text{FS}}(Y, Q)$ in Eq. 10 is restricted to the factor $J_{\text{IA}}(Y')$, through the one-body density matrix $\tilde{n}(s)$.

Figure 2b compares the predictions of the Silver and Carraro–Koonin at a wavevector $Q = 27.0 \text{ \AA}^{-1}$ and the equilibrium number density $\rho = 0.0217 \text{ \AA}^{-3}$. Both models consist of a central peak and damped oscillatory tails which are both positive and negative. They obey the normalization, f -sum rule, and ω^2 -sum rule conditions. The central peak of $R_{\text{CK}}(Y, Q)$ (FWHM $\approx 0.8 \text{ \AA}^{-1}$) is broader than that of $R_{\text{S}}(Y, Q)$ (FWHM $\approx 0.6 \text{ \AA}^{-1}$). The oscillatory tails of the two theories are out of phase, and they have different frequencies and amplitudes.

The expected intrinsic scattering $J_{\text{FS}}(Y, Q)$ is obtained by convoluting the QMC calculations of $J_{\text{IA}}(Y)$ with the FSE broadening functions. Figure 2c illustrates the anticipated scattering, including the effects of instrumental resolution, at $T = 1.09 \text{ K}$ and $Q = 27.0 \text{ \AA}^{-1}$. Despite obvious differences between the Silver and Carraro–Koonin theories, their predictions are similar. The lineshape is broad and featureless: the condensate peak has entirely disappeared. Small differences in the predicted lineshape will be undetectable in the presence of statistical noise. The only practically observable difference between the Silver and Carraro–Koonin theories occurs near $Y = +2 \text{ \AA}^{-1}$.

Finally, we note the IA is approached slowly as a function of Q in liquid ^4He . The atom–atom scattering cross section $\sigma(Q)$ in a liquid composed of infinitely hard spheres is independent of Q . In such an idealized liquid, the neutron Compton profile $J(Y, Q)$ would Y -scale even though the IA-limit would never be reached [69]. The real interatomic potential of liquid ^4He does not contain an infinitely hard core. Nevertheless, the interatomic potential is exponentially repulsive at short distances. As a result, the ^4He - ^4He scattering cross section $\sigma(Q)$ varies as $\log Q$, apart from glory oscillations [43, 58]. Therefore, Y -scaling should hold, to good approximation, over a limited range in Q , although the scaling function will not be $J_{\text{IA}}(Y)$.

3 Experimental Approach

3.1 Experimental Details

We carried out a neutron Compton scattering study of liquid ^4He using the ARCS spectrometer [70–72] at the Spallation Neutron Source. This instrument is a direct geometry, time-of-flight spectrometer. Incident neutron energies between 15–5000 meV are available from the decoupled poisoned water moderator. A T_0 chopper, operating at a frequency of 180 Hz, blocks the burst of prompt radiation released from the source when the protons hit the target. An incident neutron energy ($E_i = 710 \text{ meV}$) is chosen by time-of-flight using the phase of a Fermi chopper rotating at 600 Hz, placed just upstream of the sample. The sample was enclosed in a cryostat which will be described shortly. Neutrons that scatter off of the sample traverse an oscillating radial collimator on their way to the detector array. There are two low efficiency beam monitors, one located after the Fermi chopper and another located just before the beam stop. The beam profile observed at these monitors is used to determine the initial neu-

tron energy E_i and moderator emission time t_0 . Complete details of the instrument are provided in Refs. [70,71].

The aforementioned sample environment consisted of an orange cryostat coupled with a custom 1 K insert. The orange cryostat cooled the insert to a temperature <3 K. The custom insert then provides a base temperatures of approximately 1 K and temperature stability of <1 mK. It consists of Al-6061 sample cell that is mechanically mounted to a 1 K pot built from oxygen-free high conductivity copper. Both are enclosed within an aluminum vacuum can isolating them from the exchange gas of the orange cryostat. The liquid ^4He within the sample cell had a height of 5.08 cm and a diameter of 2.54 cm. We estimate that the beam transmission is approximately 94% given the sample geometry. Two temperature control packages, consisting of a heater and a germanium semiconductor thermometer, were attached to the insert, one to the 1 K pot and the other to the bottom of the sample cell. The temperature stability was obtained by operating each package on an independent temperature control loop. Each thermometer was calibrated to ± 4 mK. Furthermore, the temperature dependence of the observed vapor pressure of the liquid ^4He in the sample cell was consistent with the semiconductor thermometry.

We collected data at a series of different sample temperatures $T = 1.090(10)$, $1.400(10)$, $1.650(4)$, $1.800(4)$, $2.000(4)$, $2.100(4)$, $2.35(30)$, and $2.650(15)$ K with measurement periods varying between 2 and 15 h. The background scattering due to the sample environment and empty sample can was measured at $2.7(1)$ K. The quoted errors in the sample temperature represent whichever quantity is larger, either the systematic uncertainty in the temperature scale or the random uncertainty from the stability of the cryogenics. No thermal gradient was observed between the bottom of the sample cell and the 1 K pot above it.

An event-based data acquisition system stores the data as list of time stamps and pixel locations. Histogramming the raw data occurs during reduction and at this step we filtered out events that occurred when the sample temperature was outside of our stability criteria [73]. The data, as counts versus time-of-flight, was then normalized to the proton charge on target to remove variation in source output. The measured double-differential cross section $d^2\sigma/d\Omega dE$ is transformed to the neutron Compton profile $J(Y, Q)$ using the Mantid and DAVE software packages [74,75]. The scattering data $J(Y, Q)$ between $20.0 \text{ \AA}^{-1} \leq Q \leq 27.5 \text{ \AA}^{-1}$ were analyzed in steps of 0.5 \AA^{-1} each having a widths of $\pm 0.2 \text{ \AA}^{-1}$.

We used two independent methods to determine the absolute intensity scale for the neutron Compton profile $J(Y, Q)$. One approach is to measure the total scattering off a standard vanadium foil having the same dimensions as the lateral surface area of the sample can, and scaling the observed double-differential cross section $d^2\sigma/d\Omega dE$ of the sample accordingly. Taking the microscopic scattering cross section of vanadium to be 421.0 mbarn/sR, the normalization factor was determined by integrating the scattering over energy transfers $-150 \text{ meV} \leq E \leq 685 \text{ meV}$ and scattering angles $10^\circ \leq \phi \leq 135^\circ$. In the second approach, we numerically integrated the neutron Compton profile $J(Y, Q)$ and imposed the zeroth moment sum rule. This method of setting an absolute intensity scale implicitly assumes that all of the nonzero parts of $J(Y, Q)$ are observed. The two methods typically produced consistent absolute intensity scales in the range of 1–10%.

When comparing the experimental data to theoretical models, we allow for a small shift Y_c in the theoretical predictions to ensure that the f -moment sum rule is satisfied. If the energy scale were perfectly defined, then Y_c would be exactly zero. However, uncertainties in the incident neutron energy E_i , moderator emission time t_0 , lengths of flight paths, and other instrument parameters can introduce small shifts to the energy scale. Typical values for Y_c are on the order of 0.01 \AA^{-1} which is less than a bin width in Y and small compared to the resolution width.

3.2 Instrumental Resolution

We calculated the instrumental resolution function $I(Y, Q)$ using a realistic Monte Carlo ray tracing simulation of the scattering experiment [76,77]. The simulations were carried out using the McStas software suite [78,79]. The input to the simulation includes the spectrum of the decoupled water moderator, the known instrument parameters, sample geometry, and a sample kernel. There were 2.8×10^{12} incident neutron pulses simulated for this calculation. The output of the simulation includes both the incident beam monitors and the scattering measured at the detector bank. The output of the simulation, as counts versus time-of-flight, receives the same treatment as the real scattering data. The effective instrumental resolution function $I(Y, Q)$ is determined from the output of the simulation by deconvoluting the known sample kernel from the simulated scattering.

An accurate description of the time-structure of the incident neutron pulse is necessary for a reliable determination of $I(Y, Q)$. We found that the McStas model reproduces the time-of-flight profiles observed by the incident beam monitors. This indicates that the instrument simulation faithfully describes the velocity-time distribution of neutrons as they emerge from the moderator and pass through the Fermi chopper.

Recent calculations of the instrumental resolution function $I(Y, Q)$ of ARCS used an ideal δ -function scatterer for the sample kernel [80]. Instead, we have chosen to base our sample kernels on previous Quantum Monte Carlo calculations of $n(k)$ [36,81]. The Isotropic_Sqw sample component was used as it allowed us to easily change models [82].

We found that the effective resolution function $I(Y, Q)$ could be described as a single Gaussian in Y . The full-width at half-maximum of $I(Y, Q)$ decreases roughly linearly from 1.05 \AA^{-1} at $Q = 20 \text{ \AA}^{-1}$ to 0.50 \AA^{-1} at $Q = 27.5 \text{ \AA}^{-1}$. Our calculated resolution functions $I(Y, Q)$ agree with the ‘observed’ ones reported in Ref. [80].

The observed Compton profile $J_{\text{EXP}}(Y, Q)$ is obtained by convoluting the intrinsic scattering with the instrumental resolution function:

$$J_{\text{EXP}}(Y, Q) = \int_{-\infty}^{+\infty} J_{\text{FS}}(Y', Q) I(Y - Y', Q) dY' \tag{12}$$

Both the instrumental resolution $I(Y, Q)$ and FSE function $R(Y, Q)$ have the effect of smearing sharp features in $J_{\text{IA}}(Y)$.

3.3 Background Subtraction and Multiple Scattering Corrections

The sample-independent background scattering was measured at 2.7(1) K. The signal is due to scattering from the sample cell, insert vacuum can, tails of the orange cryostat, and dark counts. At the wavevectors considered in the data analysis, $20.0 \text{ \AA}^{-1} \leq Q \leq 27.5 \text{ \AA}^{-1}$, the helium recoil peak is either mostly or completely separated from the elastic Bragg scattering and heavy element recoil lines present in the background. The signal-to-background ratio in the region of the helium peak is very high.

We find that a sample-dependent residue remains after the subtraction of the background signal. This component of the measured signal is due to the multiple scattering of neutrons. It is approximately constant with scattering angle and forms a broad band in the energy spectrum, being centered at 300 meV and having a FWHM of 380 meV. The intensity of the multiple scattering is only a few percent of the intensity of the helium peak.

Here we make the assumption that the multiple scattering is isotropic and additive. Because the multiple scattering at low Q is clearly separated from the helium recoil line, we fit the multiple scattering component at low Q to a smooth curve and subtracted this smooth curve from the experimental data at all values of Q .

4 Experimental Results

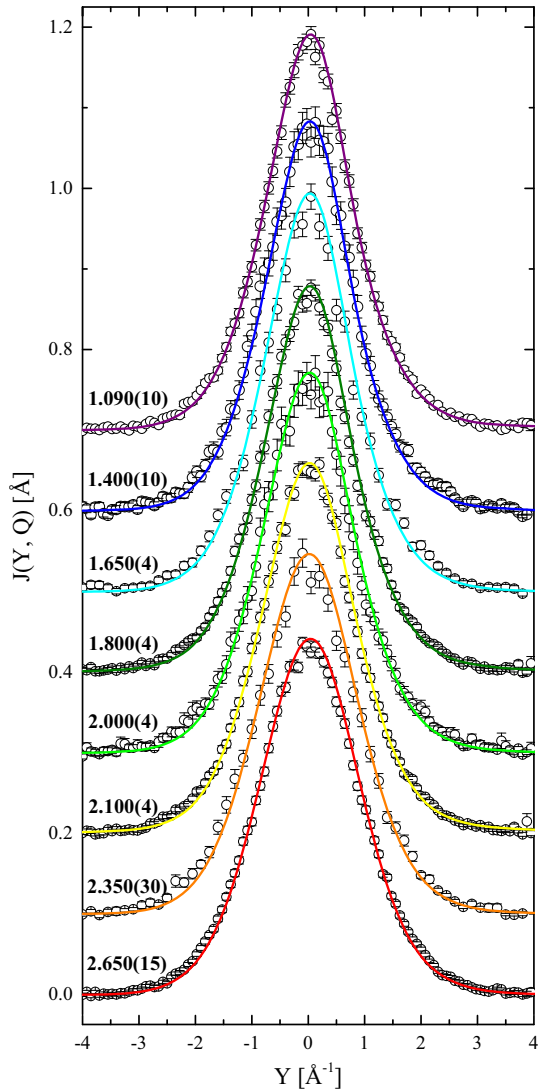
Figure 3 plots the neutron Compton profile $J(Y, Q)$ observed at $Q = 27.0 \text{ \AA}^{-1}$ as a function of temperature. The observed scattering $J(Y, Q)$ consists of a single, non-Gaussian peak containing no sharp features or oscillations. The overall width of the scattering, $\approx 2 \text{ \AA}^{-1}$, is dominated by quantum-mechanical zero-point motion. It is also much broader than the instrumental resolution width, 0.55 \AA^{-1} , at this Q .

We find that the scattering is only weakly dependent on temperature in the normal fluid phase. When the temperature is reduced below T_λ , the scattering $J(Y, Q)$ becomes visibly narrower and more peaked. This increase in scattering at small Y below T_λ is consistent with the existence of a Bose condensate peak located at $Y = 0$ which has been broadened by finite instrumental resolution and FSE. However, as shown below, the scattering data is also consistent with models that do not include a Bose condensate. The scattering data does not, by itself, prove that a Bose condensate is present below T_λ .

Y -scaling behavior is observed at all temperatures considered in this study. To illustrate, Fig. 4 overplots the scattering in the normal and superfluid phases. In both cases, the scattering clearly collapses onto a single curve.

One might be tempted to conclude from this fact that the IA-regime has been reached in this experiment. We stress that Y -scaling is a necessary, but not sufficient, condition for the IA. Because FSE in liquid ^4He vary as $\log(Q)$, they are expected to not change appreciably over less than a decade in Q . As a result, the scattering data obeys Y -scaling to good approximation, even though the scaling function is not $J_{\text{IA}}(Y)$.

Fig. 3 The neutron Compton profile $J(Y, Q)$ at $Q = 27 \text{ \AA}^{-1}$. The different temperature data sets have been vertically offset by 0.1 \AA . The *solid lines* represent our QMC calculations folded with the instrumental resolution function $I(Y, Q)$ the final state effect function $R(Y, Q)$ of Carraro–Koonin. Throughout the paper, *error bars* on the scattering data represent one standard deviation (Color figure online)



5 Discussion

5.1 Lineshape Comparison

Theoretical calculations of the momentum distribution $n(k)$ may be checked for their consistency with the scattering data, even if the Bose condensate peak does not appear as a distinct feature in $J(Y, Q)$. To make the most stringent possible test, one should compare the entire predicted lineshape for $J(Y, Q)$ with the neutron Compton scattering data. The solid lines in Fig. 3 are obtained when our QMC calculations of $J_{IA}(Y)$ are convoluted with final state effects $R_{CK}(Y, Q)$ and instrumental resolution $I(Y, Q)$.

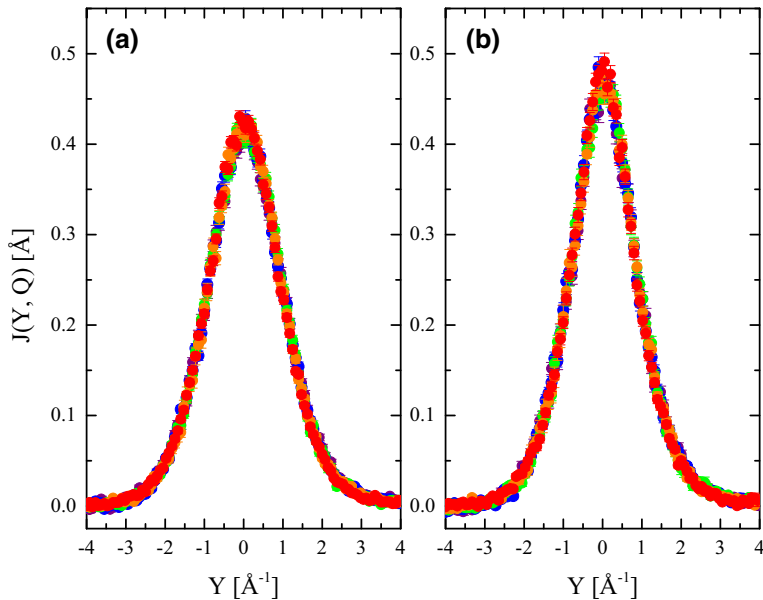


Fig. 4 Test of Y-scaling at (a) 2.650(15)K and (b) 1.090(10)K. Points: $Q = 23.0 \text{ \AA}^{-1}$ (purple), 24.0 \AA^{-1} (blue), 25.0 \AA^{-1} (green), 26.0 \AA^{-1} (orange), 27.0 \AA^{-1} (red) (Color figure online)

We have allowed the amplitude and center position Y_c of the predicted scattering to vary, but not the shape of the peak. As can be seen, there is excellent agreement between the predicted and observed lineshapes at all temperatures. The same level of agreement is obtained at other values of Q . This convergence between ab initio predictions and the measured scattering is strong evidence that a Bose broken symmetry is responsible for the superfluid phase transition of liquid ^4He .

In making this comparison, we are testing the combination of the QMC calculations and the Carraro–Koonin theory. The scattering data, when corrected for instrumental resolution, only provides information about $J_{\text{FS}}(Y, Q)$. It does not provide information about the IA-scattering $J_{\text{IA}}(Y)$ or FSE function $R(Y, Q)$ considered separately. If one assumes that the FSE function $R(Y, Q)$ is known, then one may test theoretical predictions for the IA-scattering $J_{\text{IA}}(Y)$ against the data. Below we will introduce parameterized models for $J_{\text{IA}}(Y)$ which permit empirical estimates for the average kinetic energy $\langle E_K \rangle$ and Bose condensate fraction n_0 .

On the other hand, one may turn this problem around, assuming that $J_{\text{IA}}(Y)$ is known and test different theories for $R(Y, Q)$ against the scattering data. Now we assume that our QMC calculations of $J_{\text{IA}}(Y)$ are correct. The solid lines in Fig. 5 compared the predicted scattering according to the Silver and Carraro–Koonin theories with the experimental data at $T = 1.09 \text{ K}$ and $Q = 27.0 \text{ \AA}^{-1}$. Overall, both theories are in excellent agreement with the scattering data. Statistical noise and instrumental resolution effects make these theories indistinguishable for most values of Y .

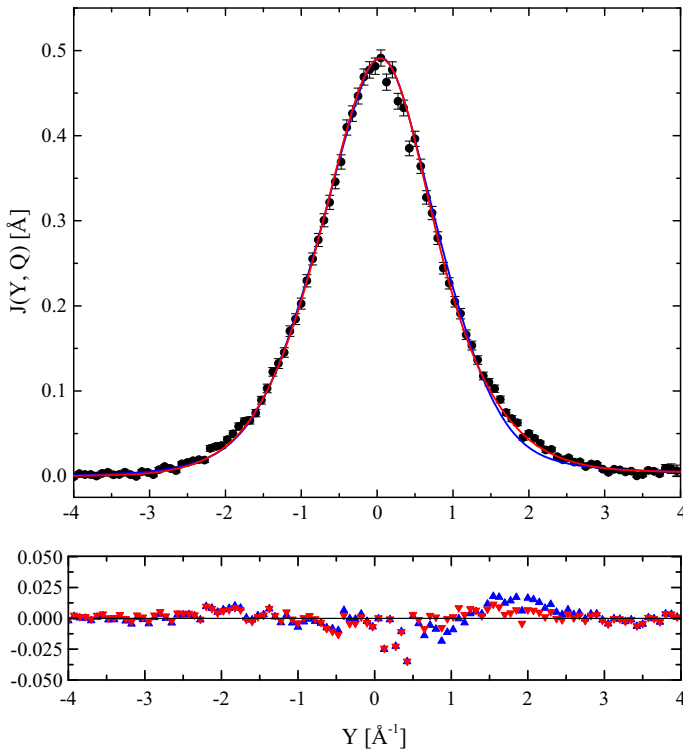


Fig. 5 The neutron Compton profile $J(Y, Q)$ at $Q = 27.0 \text{ \AA}^{-1}$ and $T = 1.090(10) \text{ K}$ is compared to theoretical predictions based on two different final state effect theories. *Main panel* experimental points (black circles); QMC calculations folded with Carraro–Koonin theory (red) and with HCPT (blue) *Lower panel* difference curves (Color figure online)

Nevertheless, it is clear from the residuals shown in Fig. 5 that the Carraro–Koonin theory offers a better description of the scattering data near $Y = +2 \text{ \AA}^{-1}$. The theoretical neutron Compton profile in this Y range is particularly sensitive to the final state effect function. For instance, using the $R(Y, Q)$ from Ref. [63], there is good general agreement with the experimental data at $Q = 23.0 \text{ \AA}^{-1}$ but neutron Compton profile is underestimated for $Y \geq 1.5 \text{ \AA}^{-1}$.

We find that Silver’s theory underestimates the scattering near $Y = +2 \text{ \AA}^{-1}$ at other temperatures T and values of Q as well. For comparison, we note that the PHOENIX group adopted Silver’s model FSE function in their comprehensive study of the ^4He phase diagram [32,33]. Those authors also found a small systematic deviation near $Y = +2 \text{ \AA}^{-1}$ when $R_S(Y, Q)$ was used to analyze the scattering data. Because the deviation was found not to depend upon the phase, temperature, density, or geometry of the sample, they attributed the small difference to the form of their model $R_S(Y, Q)$ [33].

5.2 Empirical Estimates of $\langle E_K \rangle$

Another approach to analyzing the scattering data is to define a parameterized model for the momentum distribution $n(k)$. The values of the adjustable parameters are estimated by means of a least-squares fit to the experimental data, taking into account the broadening of the IA-scattering by instrumental resolution $I(Y, Q)$ and final state effects $R(Y, Q)$. One thereby extracts several parameters from the experimental data, such as the average kinetic energy $\langle E_K \rangle$ or the Bose condensate fraction n_0 , to compare to theoretical predictions.

We first employ the phenomenological model developed by Sosnick et al. [31,33] to obtain empirical estimates for $\langle E_K \rangle$ as a function of temperature. Their model momentum distribution $n(k)$ consists of a sum of two Gaussians:

$$n_P(k) = \sum_{i=1}^2 \frac{A'_i}{(2\pi\sigma_i^2)^{3/2}} e^{-k^2/2\sigma_i^2} \quad (13)$$

where the integrated intensities, A'_1 and A'_2 , add to unity. This is a physically reasonable model for a cold quantum liquid where both particle statistics and zero-point motion are important. It satisfies physical constraints such as being normalized, positive-definite, isotropic, and symmetric about $k = 0$. The IA-scattering in this model is also given by a sum of two Gaussians:

$$J_{\text{IA}}^{(P)}(Y) = \sum_{i=1}^2 \frac{A_i}{(2\pi\sigma_i^2)^{1/2}} e^{-(Y-Y_c)^2/2\sigma_i^2} + aY + b \quad (14)$$

The two Gaussians are locked to a common center Y_c . We have included the linear background in order to account for any multiple scattering that is not fully removed by our subtraction procedure. The average kinetic energy is given by: $\langle E_K \rangle = (3\hbar^2/2m)(A_1\sigma_1^2 + A_2\sigma_2^2)/(A_1 + A_2)$.

The observed neutron Compton profile $J(Y, Q)$ was fit using the phenomenological model $J_{\text{IA}}^{(P)}(Y)$ at all wavevectors Q and temperatures T . Figure 6 plots a representative fit to the scattering data at $Q = 26.5 \text{ \AA}^{-1}$ and $T = 1.800(4) \text{ K}$. The scattering data has been plotted as $\log(J(Y, Q))$ vs Y^2 to illustrate each Gaussian component in the fit. The small linear background due to multiple scattering has been subtracted. Typical values of χ^2 are close to one, and the difference curves reveal no systematic discrepancies between the model and the scattering data.

Figure 7 illustrates the kinetic energies $\langle E_K \rangle$ extracted from $J(Y, Q)$ as a function of Q . The observed kinetic energy is constant with Q , as required by the ω^2 -sum rule. The best estimate for the kinetic energy $\langle E_K \rangle$ is obtained by combining the results of these measurements at each Q by means of a weighted average. Experimental estimates for the average kinetic energy $\langle E_K \rangle$ are listed in Table 1. Equivalent results for $\langle E_K \rangle$ are obtained when $J_{\text{IA}}^{(P)}(Y)$ is broadened only by the instrumental resolution function and when it is broadened by both the resolution and final state effects. This is due to the fact that $\langle E_K \rangle$ is determined by only the intrinsic (i.e., resolution corrected)

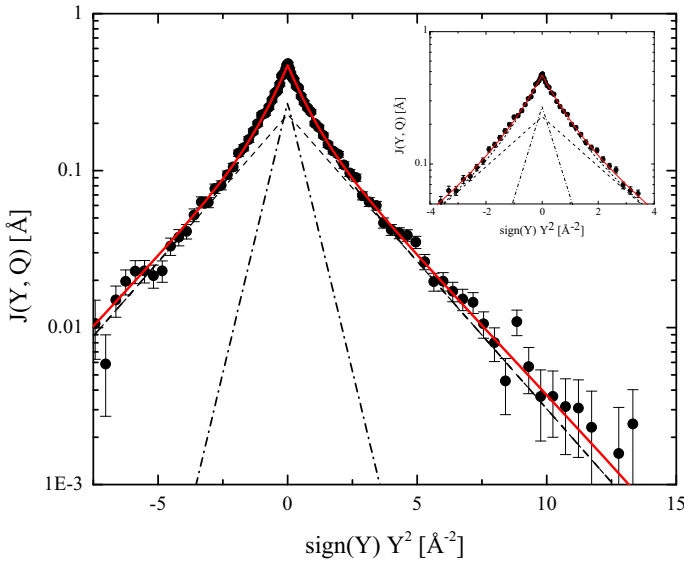


Fig. 6 The observed scattering at $Q = 26.5 \text{ \AA}^{-1}$ and $T = 1.800(4) \text{ K}$. The *red curve* is the result of fitting to the phenomenological model $J_{IA}(Y)$ as described in the main text. The *dashed* and *dash-dot* lines are the two Gaussian components. The value of χ^2 is 1.006 (Color figure online)

second moment of the scattering. Therefore, these empirical estimates may be viewed as model-independent.

Theoretical and experimental values for the average kinetic energy $\langle E_K \rangle$ of liquid ^4He under SVP are shown in Figure 8. The QMC calculations predict that $\langle E_K \rangle$ increases from 14.17(2) K at 1.09 K to 15.39(5) K at 2.100 K. The kinetic energy increases rapidly through the superfluid phase transition at T_λ , reaching a relatively constant value of $\approx 16.2 \text{ K}$ in the normal liquid. The QMC calculations are in excellent agreement with the ARCS data set presented in this paper, as well as previous investigations using the MARI [25, 26] and eVS [35] spectrometers.

The measured scattering from liquid ^4He is consistent with many possible forms for the momentum distribution $n(k)$. In Sect. 5.1, we showed that ab initio calculations of $J(Y, Q)$ are in agreement with the observed scattering. These calculations predict a finite Bose condensate fraction n_0 in the superfluid phase. However, the observed scattering is also consistent with models that do not incorporate a Bose condensate in the superfluid phase, such as the phenomenological model. This is consistent with the PHOENIX and MARI groups who both report that their scattering data may be fit to models where n_0 is zero [26, 31]. Sivia and Silver have shown that the problem of directly inverting the scattering data $J(Y, Q)$ to a unique momentum distribution $n(k)$ is ill-posed [83]. Prior knowledge in the form of a physical model is necessary to obtain empirical estimates of the condensate fraction n_0 .

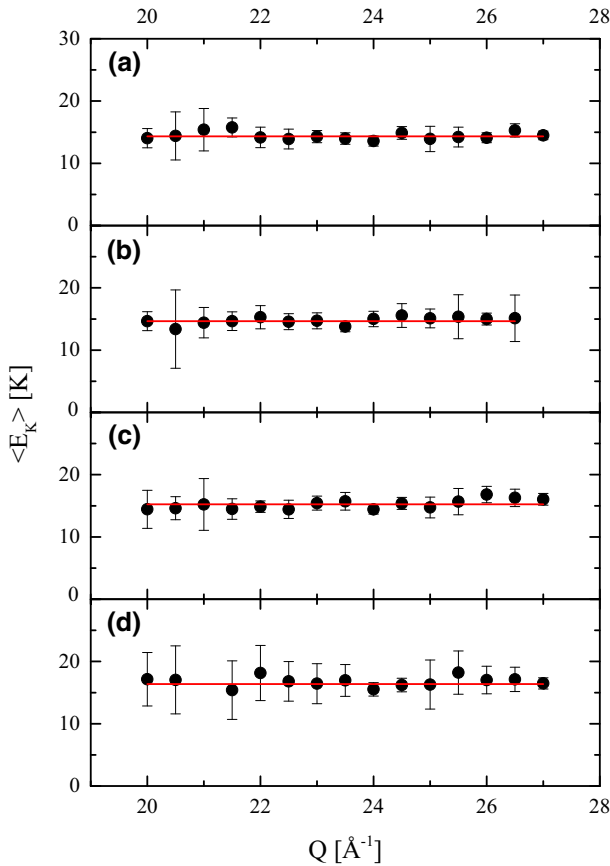


Fig. 7 Experimental estimates for the average atomic kinetic energy (E_K) obtained from the phenomenological model $J_{IA}(Y)$: **a** 1.090(10) K, **b** 1.800(4) K, **c** 2.100(4) K, and **d** 2.650(15) K. The best estimate for $\langle E_K \rangle$ at each temperature is shown by a horizontal red line (Color figure online)

5.3 Empirical Estimates of n_0

In this section, we obtain empirical estimates of the Bose condensate fraction n_0 as a function of temperature. We introduce two different parameterized expressions for the IA-scattering $J_{IA}(Y)$ that explicitly incorporate a Bose condensate. Both models are broadened by instrumental resolution $I(Y, Q)$ and final state effects $R_{CK}(Y, Q)$ when fitting the scattering data.

Model A: Expansion in Orthogonal Polynomials The first model represents the momentum distribution $n(k)$ as the sum of a δ -function singularity plus a non-Gaussian peak [23].

$$n(\mathbf{k}) = n_0\delta(\mathbf{k}) + (1 - n_0)\frac{e^{-k^2/2\sigma^2}}{(2\pi\sigma^2)^{3/2}} \left(1 + \sum_{n=2}^{\infty} a_n(-1)^n L_n^{1/2} \left(\frac{k^2}{2\sigma^2} \right) \right) \quad (15)$$

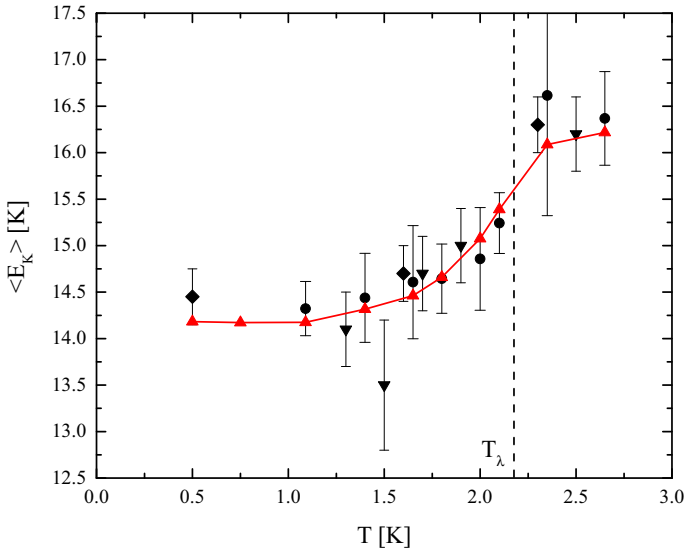


Fig. 8 The average atomic kinetic energy $\langle E_K \rangle$ of liquid ${}^4\text{He}$ under saturated vapor pressure. Experimental estimates: present ARCS study (circles), MARI [25,26] (diamonds), and eVS [35] (triangles). Our QMC predictions are shown as red triangles, the line being a guide to the eye (Color figure online)

Here $L_n^{1/2}$ is an associated Laguerre polynomial of order n . When transformed into the Y -coordinates, Model A has the following form:

$$J_{IA}(Y) = n_0\delta(Y - Y_c) + (1 - n_0)\frac{e^{-(Y-Y_c)^2/2\sigma^2}}{\sqrt{2\pi\sigma^2}} \left[1 + \sum_{n=2}^{\infty} a_n \frac{1}{2^{2n}n!} H_{2n} \left(\frac{Y - Y_c}{\sigma\sqrt{2}} \right) \right] + aY + b \tag{16}$$

Here H_n is the Hermite polynomial of order n . An overall scale factor is also included to allow for uncertainty in the absolute intensity scale. The second moment of the scattering is equal to $(1 - n_0)\sigma^2$. Nonzero values of the expansion coefficients $\{a_n\}$ do not affect the second moment of $J_{IA}(Y)$. Again, we include a linear background to account for residual multiple scattering in the tails of $J(Y, Q)$.

When fitting the scattering data, we have kept n_0 , σ , and as few expansion coefficients $\{a_n\}$ needed to obtain a χ^2 of approximately unity. Only terms up to a_4 were kept.

Model B: Cumulant Expansion The second model represents the momentum distribution $n(k)$ in terms of a cumulant expansion [22]. The momentum distribution is expressed as a sum of three terms:

$$n(\mathbf{k}) = n_0(\delta(\mathbf{k}) + f(k)) + A_1n^*(k) \tag{17}$$

The first term is the δ -function singularity of the condensate itself. The second term, $n_0 f(k)$, is the weaker singularity produced by the coupling of virtual phonons with the condensate.

$$f(k) = \frac{1}{(2\pi)^3} \frac{mc}{2\hbar\rho} \frac{1}{k} [2N(c\hbar k) + 1] e^{-k^2/k_c^2}. \tag{18}$$

Here, m is the mass of a helium atom; ρ is the number density of the liquid; c is the phonon velocity; and N is the Bose population factor. If $\hbar ck \gg k_B T$, then $f(k)$ is proportional to $1/k$; if $\hbar ck \ll k_B T$, then $f(k)$ is proportional to $1/k^2$. The exponential e^{-k^2/k_c^2} is introduced ad hoc to smoothly cut off the contribution of $f(k)$ outside the phonon region. Following the literature [22], we fix $k_c = 0.5 \text{ \AA}^{-1}$.

The third term $A_1 n^*(k)$ is the momentum distribution of the atoms above the condensate. They are described by a cumulant expansion:

$$\tilde{n}^*(s) = \exp \left[\sum_{n=2}^{\infty} \alpha_n \frac{(is)^n}{n!} \right] \approx \exp \left[-\frac{\alpha_2 s^2}{2!} + \frac{\alpha_4 s^4}{4!} - \frac{\alpha_6 s^6}{6!} \right] \tag{19}$$

Here $\tilde{n}^*(s)$ is the Fourier transform of $n^*(k)$. The prime indicates that only terms with even n contribute. The coefficients α_n of the expansion are the statistical cumulants of $n^*(k)$.

There is no simple analytic expression for $J_{IA}(Y)$ when terms up to α_6 are retained.

$$J_{IA}(Y) = n_0(\delta(Y - Y_c) + \bar{f}(Y - Y_c)) + A_1 \bar{J}^*(Y - Y_c) + aY + b \tag{20}$$

Here the overbar signifies the result of transforming $f(k)$ and $n^*(k)$ into the Y -scaling variable. The adjustable parameters describing the momentum distribution are: n_0 , α_2 , α_4 , and α_6 .

Overlap between the models These two models for $J_{IA}(Y)$ appear to treat the uncondensed part of the momentum distribution $n(k)$ very differently. However, there is a special case where they are exactly equivalent. If the higher order cumulants are small, then $\tilde{n}^*(s)$ can be approximated as follows:

$$\tilde{n}^*(s) \approx \exp \left[-\frac{\alpha_2 s^2}{2} \right] \left(1 + \frac{\alpha_4 s^4}{4!} \right) \tag{21}$$

In this particular case, the characteristic function $\tilde{n}^*(s)$ transforms analytically:

$$J_{IA}^*(Y) = \frac{1}{\sqrt{2\pi\sigma^2}} \exp \left[-\frac{Y^2}{2\sigma^2} \right] \left(1 + \frac{\delta}{8} \left(1 - \frac{2Y^2}{\sigma^2} + \frac{Y^4}{3\sigma^4} \right) \right) \tag{22}$$

Here $\sigma^2 = \alpha_2$ and $\delta = \alpha_4/\alpha_2^2$. This expression, Eq. 22, is equivalent to keeping only H_4 in Eq. 16 with $\delta = 3\alpha_2$.

We have used the full expression in Eq. 20 to fit the scattering in almost all of the data sets. However, given the statistical noise in the 1.40 K data measurements, we have used Eq. 22 to represent the uncondensed part of $n(k)$.

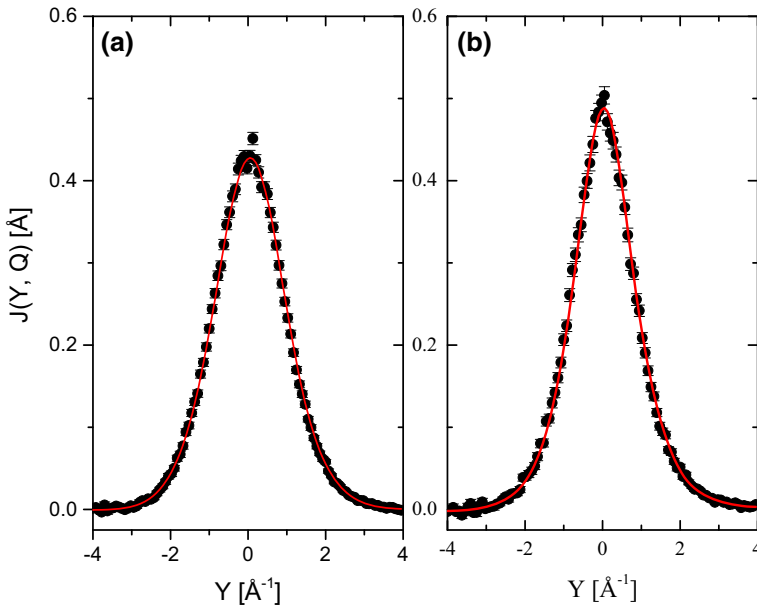


Fig. 9 The observed scattering for $Q = 26.5 \text{ \AA}^{-1}$ is fit to Model B at **a** 2.650(10)K and **b** 1.090(10)K. From the fit shown in **a**, we find that $n_0 = 0.000(9)$, $\alpha_2 = 0.90(2) \text{ \AA}^{-2}$, and χ^2 is 0.975 at this Q . Meanwhile, the fit shown in **b** yields $n_0 = 0.068(7)$, $\alpha_2 = 0.87(3) \text{ \AA}^{-2}$, and χ^2 is 0.866 for this Q (Color figure online)

Results of the Fits We fit the scattering data $J(Y, Q)$ at all temperatures T using Model A and Model B, with the exception of the 2.35 K data set, where the statistical precision of the data is too low to obtain a meaningful estimate of n_0 . Figure 9 shows representative fits to the scattering data using Model B. Typical values of χ^2 are close to unity and the residuals do not indicate any systematic discrepancies between the model curve and the scattering data.

Figure 10 plots the values of n_0 and α_2 obtained at $T = 1.090(10)$ K. The observed values of the condensate fraction n_0 and second cumulant α_2 are independent of Q . The best estimate for these quantities is obtained by taking a weighted average over all values of Q . For this temperature, we obtained $n_0 = 0.070(4)$ and $\alpha_2 = 0.859(10) \text{ \AA}^{-2}$. The average kinetic energy $\langle E_K \rangle$ is 14.2(2) K, which is consistent with the result of the phenomenological model.

Empirical estimates for the condensate fraction n_0 obtained from the ARCS data set are listed in Table 2. We have also carried out the same analysis upon the PHOENIX data sets [31, 33]. These results are shown in Table 3. Consistent results are obtained from the ARCS and PHOENIX data sets when common models are used to analyze the scattering data.

Figure 11 plots empirical estimates of n_0 obtained from the ARCS, MARI, and PHOENIX spectrometers. These values are compared with our present (QMC) estimates for n_0 , which are obtained by averaging the value of the one-body density matrix $\tilde{n}(s)$ at distances above 7 Å. Also shown is a ground state QMC prediction [49].

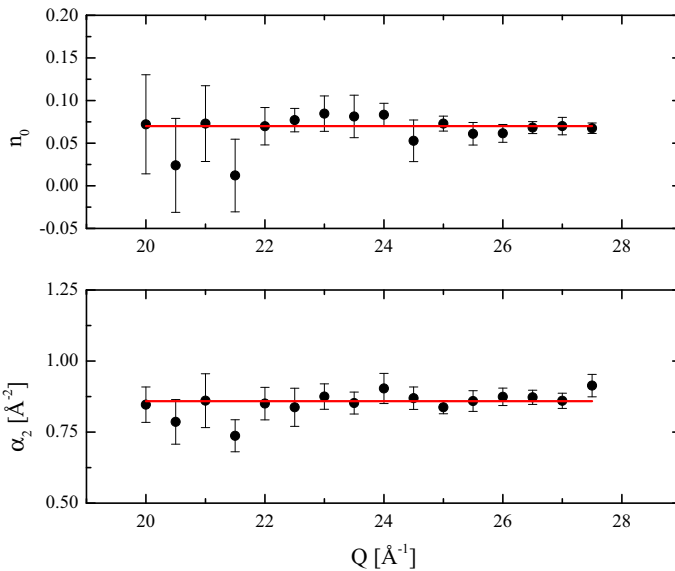


Fig. 10 Experimental estimates for the condensate fraction n_0 and the second cumulant α_2 obtained from the $T = 1.090(10)$ K data set using Model B described in the text. The best estimate for each quantity is shown by a horizontal red line (Color figure online)

Table 3 Values of the condensate fraction n_0 estimated from the PHOENIX data set

T (K)	Model A	Model B
0.32	0.071(9)	0.070(5)
1.00	0.069(9)	0.070(5)
1.50	0.069(9)	0.065(5)
1.80	0.045(9)	0.055(5)
2.00	0.042(14)	0.033(5)
2.30	0.000(2)	0.000(19)
2.80	0.001(4)	0.000(4)
3.50	0.000(1)	0.000(11)

Another recent theoretical calculation places the ground state value slightly higher, namely $n_0 = 0.0801(22)$ [84]. At low temperatures, the condensate fraction is close to 7.5%. No significant temperature dependence is observed below 1.1 K. However, above 1.1 K, the condensate fraction n_0 decreases rapidly toward zero as the transition temperature T_λ is approached. In the normal fluid phase, the condensate fraction n_0 is zero.

The relationship between the phonon-roton spectrum and the Bose condensate in superfluid ^4He is presently an open question. Giorgini et al. [85] proposed that the thermal excitation of rotons is the chief mechanism driving the depletion of the condensate as the temperature approaches T_λ . According to their theory, the ground state value of the condensate fraction $n_0(0)$ is driven by the smallness of the ratio

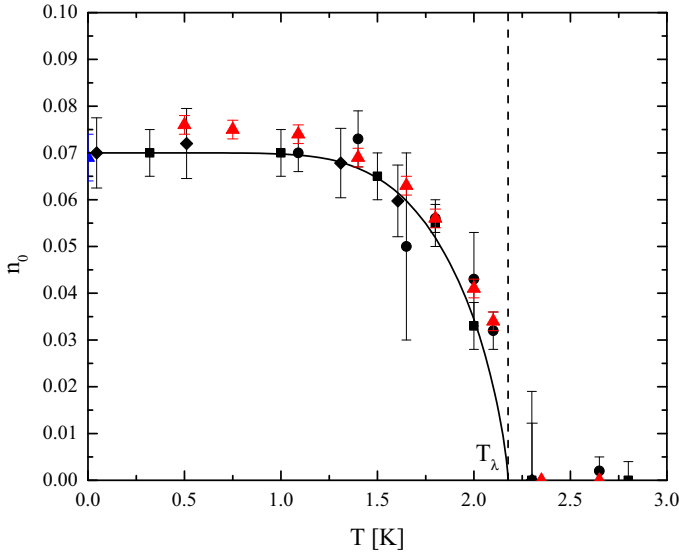


Fig. 11 The Bose condensate fraction n_0 of liquid ^4He under saturated vapor pressure. Experimental estimates: present ARCS study (*circles*), MARI (*diamonds*), and our re-analysis of the PHOENIX data set (*squares*). Theoretical points: current QMC estimates (*red triangle*), Reptation Quantum Monte Carlo (*blue triangle*), and the GPS theory (*solid black line*) (Color figure online)

$3k_B T_\lambda m / \hbar^2 Q_R^2 \approx 0.15$, where Q_R is the roton wavevector. If $\rho_n(T)$ is the normal fluid fraction at temperature T , then they predict that the temperature dependence of the condensate fraction $n_0(T)$ is:

$$n_0(T) = n_0(0) \left(1 - \frac{T}{T_\lambda} \rho_n(T) \right) \tag{23}$$

The solid line in Fig. 11 is obtained by setting $n_0(0)$ equal to 7%. There is good agreement between the experimental data and the predictions of Eq. 23.

The estimated values of n_0 obtained from the eVS (now VESUVIO) instrument, a nuclear resonance foil spectrometer, have not been shown in Fig. 11. The eVS group [35] reports that n_0 is zero at 2.5 K. They also claim that the condensate fraction n_0 increases from 0.10(4) at 1.9 K to 0.15(4) at 1.3 K. Their values for n_0 in the superfluid phase are inconsistent with the ARCS, PHOENIX, and MARI data sets, as well QMC predictions, at the level of 1σ . We believe that the origin of this discrepancy is the comparatively coarse energy resolution that was available to the eVS group. For example, those authors note that the use of the U-foil analyzer produces a resolution function $I(Y, Q)$ having a central Gaussian width of 1.53 \AA^{-1} and Lorentzian tails of width 1.46 \AA^{-1} when $Q = 152 \text{ \AA}^{-1}$. This excludes the possibility of a detailed lineshape analysis as the intrinsic width of the scattering is approximately 2 \AA^{-1} .

6 Conclusions

In this paper, we presented a coordinated experimental and theoretical study of the momentum distribution $n(k)$, including the Bose condensate, of liquid ^4He as the superfluid transition temperature is approached. To make a rigorous comparison, the measurements were conducted under fine temperature control and Quantum Monte Carlo calculations of the momentum distribution $n(k)$ and final state effects $R(Y, Q)$ were performed for the temperature and density conditions of the experiment.

We find that there is excellent agreement between the observed neutron Compton profile $J(Y, Q)$ and ab initio predictions of its lineshape. We also used model fit functions to obtain empirical estimates of the Bose condensate fraction n_0 and average kinetic energy $\langle E_K \rangle$ as a function of temperature. These quantities, too, are in agreement with theoretical estimates. They also provide independent confirmation of the low temperature estimates obtained by the MARI group. We have compared the final state effect theories of Silver and Carraro–Koonin with our scattering data. While both theories are in good overall agreement with the observed $J(Y, Q)$, the Carraro–Koonin theory provides an improved description of the scattering in the wings of the data. Finally, upon re-analysis, we find that the ARCS and PHOENIX data sets yield consistent values of n_0 when analyzed according to the models discussed in this paper.

The convergence between the scattering data and Quantum Monte Carlo calculations is a compelling confirmation that accurate theoretical values of n_0 can be obtained using the continuous space worm algorithm, even as the temperature approaches T_λ .

Acknowledgements The authors are grateful to David Sprinkle of Indiana University for lending his expertise to the design, construction, and testing of the cryogenics built for this study. Saad Elorfi and Mark Loguillo of the Spallation Neutron Source provided technical support for this experiment. We also recognize helpful scientific discussions with Doug Abernathy, Richard Azuah, Souleymane Diallo, Jiao Lin, Matthew Stone, and Peter Willendrup. This report was prepared, in part, by Indiana University under award 70NANB10H255 from the National Institute of Standards and Technology. Matthew S. Bryan acknowledges support under NSF grant DGE-1069091. This research at ORNL's Spallation Neutron Source was sponsored by the Scientific User Facilities Division, Office of Basic Energy Sciences, U.S. Department of Energy, as well as by the Natural Science and Engineering Research Council of Canada. Computing support from Westgrid is gratefully acknowledged.

References

1. L. Pitaevskii, S. Stringari, *Bose–Einstein Condensation* (Oxford University Press, Oxford, 2016)
2. P. Pines, P. Nozieres, *Theory of Quantum Liquids: Superfluid Bose Liquids* (Westview Press, Boulder, 1999)
3. P.W. Anderson, *Basic Notions of Condensed Matter Physics*, 2nd edn. (Westview Press, Boulder, 1997)
4. A. Griffin, D.W. Snoke, S. Stringari, *Bose–Einstein Condensation* (Cambridge University Press, Cambridge, 1995)
5. A. Griffin, T. Nikuni, E. Zaremba, *Bose-Condensed Gases at Finite Temperatures* (Cambridge University Press, Cambridge, 2009)
6. D. Snoke, *Science* **298**(5597), 1368 (2002)
7. R. Balili, V. Hartwell, D. Snoke, L. Pfeiffer, K. West, *Science* **316**(5827), 1007 (2007)
8. J. Kasprzak, M. Richard, S. Kundermann, A. Baas, P. Jeambrun, J.M.J. Keeling, F.M. Marchetti, M.H. Szymanska, R. Andre, J.L. Staehli, V. Savona, P.B. Littlewood, B. Deveaud, L.S. Dang, *Nature* **443**, 409 (2006)
9. T. Nikuni, M. Oshikawa, A. Oosawa, H. Tanaka, *Phys. Rev. Lett.* **84**, 5868 (2000)

10. S.O. Demokritov, V.E. Demidov, O. Dzyapko, G.A. Melkov, A.A. Serga, B. Hillebrands, A.N. Slavin, *Nature* **443**, 430 (2006)
11. H. Deng, H. Haug, Y. Yamamoto, *Rev. Mod. Phys.* **82**, 1489 (2010)
12. J. Klaers, J. Schmitt, F. Vewinger, M. Weitz, *Nature* **468**, 545 (2010)
13. I. Carusotto, C. Ciuti, *Rev. Mod. Phys.* **85**, 299 (2013)
14. V. Graber, N. Andersson, M. Hogg, *Int. J. Mod. Phys. D* **0**, 1730015 (2017)
15. T. van Zoest, N. Gaaloul, Y. Singh, H. Ahlers, W. Herr, S.T. Seidel, W. Ertmer, E. Rasel, M. Eckart, E. Kajari, S. Arnold, G. Nandi, W.P. Schleich, R. Walsler, A. Vogel, K. Sengstock, K. Bongs, W. Lewoczko-Adamczyk, M. Schiemangk, T. Schuldt, A. Peters, T. Könemann, H. Müntinga, C. Lämmerzahl, H. Dittus, T. Steinmetz, T.W. Hänsch, J. Reichel, *Science* **328**(5985), 1540 (2010)
16. D. O'Dell, S. Giovanazzi, G. Kurizki, V.M. Akulin, *Phys. Rev. Lett.* **84**, 5687 (2000)
17. N.H. Lindner, A. Peres, *Phys. Rev. A* **71**, 024101 (2005)
18. P.C. Hohenberg, P.M. Platzman, *Phys. Rev.* **152**, 198 (1966)
19. P. Martel, E.C. Svensson, A.D.B. Woods, V.F. Sears, R.A. Cowley, *J. Low Temp. Phys.* **49**, 279 (1976)
20. E.C. Svensson, Los Alamos Report No. LA-10227-C, vol 2, p. 456 (1984)
21. R.N. Silver, P.E. Sokol, *Momentum Distributions* (Plenum Press, New York and London, 1989)
22. H.R. Glyde, *Excitations in Liquid and Solid Helium* (Clarendon Press, Oxford, 1995)
23. C. Andreani, D. Colognesi, J. Mayers, G.F. Reiter, R. Senesi, *Adv. Phys.* **54**, 377 (2005)
24. R.T. Azuah, W.G. Stirling, H.R. Glyde, P.E. Sokol, S.M. Bennington, *Phys. Rev. B* **51**, 605 (1995)
25. R.T. Azuah, W.G. Stirling, H.R. Glyde, M. Boninsegni, P.E. Sokol, S.M. Bennington, *Phys. Rev. B* **56**, 14620 (1997)
26. H.R. Glyde, R.T. Azuah, W.G. Stirling, *Phys. Rev. B* **62**, 14337 (2000)
27. H.R. Glyde, S.O. Diallo, R.T. Azuah, O. Kirichek, J.W. Taylor, *Phys. Rev. B* **84**, 184506 (2011)
28. S.O. Diallo, J.V. Pearce, R.T. Azuah, O. Kirichek, J.W. Taylor, H.R. Glyde, *Phys. Rev. Lett.* **98**, 205301 (2007)
29. S.O. Diallo, J.V. Pearce, R.T. Azuah, H.R. Glyde, *Phys. Rev. Lett.* **93**, 075301 (2004)
30. T.R. Sosnick, W.M. Snow, R.N. Silver, P.E. Sokol, *EPL* **9**, 707 (1989)
31. T.R. Sosnick, W.M. Snow, P.E. Sokol, *Phys. Rev. B* **41**, 11185 (1990)
32. W.M. Snow, Y. Wang, P.E. Sokol, *EPL* **19**, 403 (1992)
33. W.M. Snow, P.E. Sokol, *J. Low Temp. Phys.* **101**, 881 (1995)
34. K.W. Herwig, P.E. Sokol, T.R. Sosnick, W.M. Snow, R.C. Bladell, *Phys. Rev. B* **41**, 103 (1990)
35. J. Mayers, C. Andreani, D. Colognesi, *J. Phys. Condens. Matter* **9**, 10639 (1997)
36. D.M. Ceperley, *Rev. Mod. Phys.* **67**, 279 (1995)
37. D.M. Ceperley, E.L. Pollock, *Phys. Rev. Lett.* **56**, 351 (1986)
38. E.L. Pollock, D.M. Ceperley, *Phys. Rev. B* **36**, 8343 (1987)
39. M. Boninsegni, N. Prokof'ev, B. Svistunov, *Phys. Rev. Lett.* **96**, 070601 (2006)
40. M. Boninsegni, N. Prokof'ev, B. Svistunov, *Phys. Rev. E* **74**, 036701 (2006)
41. T.E. Mason, D. Abernathy, I. Anderson, J. Ankner, T. Egami, G. Ehlers, A. Ekkebus, G. Granroth, M. Hagen, K. Herwig, J. Hodges, C. Hoffmann, C. Horak, L. Horton, F. Klöse, J. Laresé, A. Mesecar, D. Myles, J. Neufeind, M. Ohl, C. Tulk, X.L. Wang, J. Zhao, *Physica B Condens. Matter* **385**, 955 (2006)
42. R.N. Silver, *Phys. Rev. B* **38**, 2283 (1988)
43. R.N. Silver, *Phys. Rev. B* **39**, 4022 (1989)
44. C. Carraro, S.E. Koonin, *Phys. Rev. Lett.* **65**, 2792 (1990)
45. S. Moroni, S. Fantoni, A. Fabrocini, *Phys. Rev. B* **58**, 11607 (1998)
46. R.P. Feynman, A.R. Hibbs, *Quantum Mechanics and Path Integrals* (McGraw-Hill, New York, 1965)
47. R.A. Aziz, V.P.S. Nain, S. Carley, W.L. Taylor, G.T. McConville, *J. Chem. Phys.* **70**, 4330 (1979)
48. Revisions of the original Aziz potential have been published over the past few decades, but the differences are relatively small, and do not affect the value of the condensate fraction to a significant degree. See, for instance, Ref. [49]
49. S. Moroni, M. Boninsegni, *J. Low Temp. Phys.* **136**, 129 (2004)
50. S. Moroni, F. Pederiva, S. Fantoni, M. Boninsegni, *Phys. Rev. Lett.* **84**, 2650 (2000)
51. F. Mezzacapo, M. Boninsegni, *Phys. Rev. Lett.* **97**, 217 (2006)
52. F. Mezzacapo, M. Boninsegni, *Phys. Rev. A* **75**, 033201 (2007)
53. C.F. Barenghi, R.J. Donnelly, *J. Chem. Phys. Ref. Data* **27**, 217 (1998)
54. K.H. Andersen, W.G. Stirling, R. Scherm, A. Stunault, B. Fak, H. Godfrin, A.J. Dianoux, *J. Phys. Condens. Matter* **6**, 821 (1994)

55. K.H. Andersen, W.G. Stirling, J. Phys. Condens. Matter **6**, 5805 (1994)
56. G. Placzek, Phys. Rev. **86**, 377 (1952)
57. V.F. Sears, Phys. Rev. B **30**, 44 (1984)
58. R. Feltgen, H. Kirst, K.A. Köhler, H. Pauly, F. Torello, J. Chem. Phys. **76**, 2360 (1982)
59. K.H. Andersen, W.G. Stirling, H.R. Glyde, Phys. Rev. B **56**, 8978 (1997)
60. H.A. Gersch, L.J. Rodriguez, Phys. Rev. A **8**, 905 (1973)
61. F. Mazzanti, J. Boronat, A. Polls, Phys. Rev. B **53**, 5661 (1996)
62. F. Mazzanti, A. Polls, J. Boronat, J. Casulleras, Phys. Rev. Lett. **92**, 085301 (2004)
63. A.S. Rinat, M.F. Taragin, F. Mazzanti, A. Polls, Phys. Rev. B **57**, 5347 (1998)
64. R.N. Silver, G. Reiter, Phys. Rev. B **35**, 3647 (1987)
65. S. Stringari, Phys. Rev. B **35**, 2038 (1987)
66. T.R. Sosnick, W.M. Snow, R.N. Silver, P.E. Sokol, Phys. Rev. B **43**, 216 (1991)
67. K.W. Herwig, P.E. Sokol, W.M. Snow, R.C. Blasdell, Phys. Rev. B **44**, 308 (1991)
68. M.S. Bryan, T.R. Prisk, R.T. Azuah, W.G. Stirling, P.E. Sokol, EPL **115**(6), 66001 (2016)
69. J.J. Weinstein, J.W. Negele, Phys. Rev. Lett. **49**, 1016 (1982)
70. D.L. Abernathy, M.B. Stone, M.J. Loguillo, M.S. Lucas, O. Delaire, X. Tang, J.Y.Y. Lin, B. Fultz, Rev. Sci. Instrum. **83**, 015114 (2012)
71. M.B. Stone, J.L. Niedziela, D.L. Abernathy, L. DeBeer-Schmitt, G. Ehlers, O. Garlea, G.E. Granroth, M. Graves-Brook, A.I. Kolesnikov, A. Podlesnyak, B. Winn, Rev. Sci. Instrum. **85**, 045113 (2016)
72. D. Abernathy, J. Niedziela, M. Stone, EPJ Web Conf. **83**, 03001 (2015)
73. P.F. Peterson, S.I. Campbell, M.A. Reuter, R.J. Taylor, J. Zikovsky, Nuclear instruments and methods in physics research section A: accelerators. Spectrom. Detect. Assoc. Equip. **803**, 24 (2015)
74. O. Arnold, J.C. Bilheux, J.M. Borreguero, A. Buts, S. Cambell, L. Chapon, M. Coucet, N. Draper, R. Ferraz Leal, M.A. Gigg, V. Lynch, A. Markvardsen, D.J. Mikkelson, R.L. Mikkelson, R. Müller, K. Palmen, P. Parker, G. Passos, T. Perring, P. Peterson, S. Ren, M.A. Reuter, A.T. Savici, J.W. Taylor, R.J. Taylor, R. Tolchenov, W. Zhou, J. Zikovsky, Nucl. Instrum. Methods Phys. Res. A **764**, 156 (2014)
75. R.T. Azuah, L.R. Kneller, Y. Qiu, P.L.W. Tregenna-Piggott, C.M. Brown, J.R.D. Copley, R.M. Dimeo, J. Res. Natl. Inst. Stand. Technol. **114**, 341 (2009)
76. G.E. Granroth, D.L. Abernathy, ICANS-XVI Proceedings, p. 289 (2003)
77. G.E. Granroth, https://github.com/granrothge/mcstas/blob/master/for_v_2/instruments/arcs_full.instr
78. K. Lefman, K. Nielsen, Neutron News **10**, 20 (1999)
79. P. Willendrup, E. Farhi, K. Lefmann, Physica B **250**, 735 (2004)
80. S. Diallo, J. Lin, D. Abernathy, R. Azuah, Nuclear instruments and methods in physics research section A: accelerators. Spectrom. Detect. Assoc. Equip. **835**, 34 (2016)
81. P. Whitlock, R. Panoff, Can. J. Phys. **65**, 1409 (1987)
82. E. Farhi, V. Hugouvieux, M. Johnson, W. Kob, J. Comput. Phys. **228**(14), 5251 (2009)
83. D.S. Sivia, R.N. Silver, in *Momentum Distributions*, ed. by R.N. Silver, P.E. Sokol (Plenum Press, Berlin, 1989), pp. 377–380
84. R. Rota, J. Boronat, J. Low Temp. Phys. **166**, 21 (2012)
85. S. Giorgini, L. Pitaevskii, S. Stringari, J. Low Temp. Phys. **89**, 449 (1992)